RSC Advances

PAPER

View Article Online
View Journal | View Issue

Cite this: *RSC Adv.*, 2021, **11**, 30487

Morphology control and interface characteristics of well-dispersed nanomaterials in K-ion batteries†

Shuya Wang,[a] Hong Zheng,*[a] Yangyang Yang,[a] Chao Liu,[a] Zhifei Pan[a] and Quanchao Zhuang*[b]

Received 23rd June 2021
Accepted 28th August 2021

DOI: 10.1039/d1ra04869d

rsc.li/rsc-advances

Potassium ion batteries (KIBs), the working mechanism of which is similar to that of lithium-ion batteries (LIBs), have drawn much interest as power sources for large-scale grid energy storage because of their low cost and abundant resources. In this paper, the feasibility of $KMnF_3$ as a cathode material for KIBs, the optimization of synthesis conditions and the interface characteristics of the charge and discharge process have been studied in detail. The study of interface characteristics is mainly done through the non-destructive test of electrochemical impedance spectroscopy (EIS).

Introduction

Recently, 3d-transition-metal binary fluorides have been extensively investigated as potential electrode materials.[1,2] The idea to exploit fluorides as batteries arose from the intrinsic stability of fluorinated materials and their ability to generate high levels of electrochemical energy. However, in LIBs and sodium-ion batteries (NIBs), transition metal binary fluorides could not be used as cathodes against a pristine carbonaceous anode, because of the lack of lithium or sodium for the current carrier.[3–5] In view of this, a lithium/sodium containing cathode is more practical. The perovskite fluorides (AMF_3, A = Li, Na, *etc.*; B = Fe, Mn, Ni, Co, Cu, *etc.*),[6,7] with the inherent three-dimensional diffusion channels and a solid structure with intersecting four-sided cavity chains,[8,9] should be of great importance in developing the next-generation Li/Na-ion batteries with large capacity. In particular, large-scale batteries are expected to become commercially viable with the use of earth-abundant transition metals.

KIBs, which have a working mechanism similar to that of LIBs, have drawn much interest as power sources for large-scale grid energy storage because of their low cost and the abundance of potassium resources.[10–12] Since perovskite fluoride had been proved to be a potential electrode material for LIBs and sodium ion batteries (NIBs), this provided a reference for studying such materials in KIBs. Due to its abundant reserves and environmental friendliness, manganese-based materials have received extensive attention as electrode materials for various types of batteries such as LIBs,[13] NIBs[14,15] and flow batteries.[16]

The key to the development of KIBs with excellent performance is to design a reasonable cathode material microstructure to achieve the ideal K ion insertion/extraction. As the cathode of KIBs, manganese-based fluoride electrode materials can overcome the shortcomings of manganese-based oxide materials ($K_{0.3}MnO_2$ (ref. 17) and $K_{0.5}MnO_2$ (ref. 18)) that cannot reach a charging voltage higher than 4 V.[19] Based on the above analysis, this paper used a manganese-based perovskite fluoride as the cathode material. Based on first-principles calculations, the possibility of perovskite fluoride $KMnF_3$ as a cathode for KIBs was predicted. To avoid the limitations of common synthetic methods of fluoride (such as high temperature, complicated procedures, and the use of corrosive hydrofluoric acid, *etc.*).[20,21] This paper used the co-precipitation method to synthesize the target material. The co-precipitation synthesis method had the characteristics of mild conditions and simple operation steps, and no surfactant or template agent is added during the synthesis process. Electrochemical impedance spectroscopy (EIS) test was used to confirm the formation process of SEI film and the main factors affecting electrochemical performance.

Experimental section

Preparation of $KMnF_3$

The perovskite fluoride $KMnF_3$ was synthesized based on the co-precipitation method. 5 mmol manganese acetate was put into the solvent to form solution, which was heated to a certain temperature. 15 mmol KF was dissolved in the solvent and then transferred to the dropping funnel. The KF solution was added dropwise to the manganese acetate solution. After the addition was complete, continue to stir for 30 minutes and settle overnight. The resulting turbid liquid was collected by centrifugation, and washed with a small amount of ethanol and water (volume ratio 1 : 1), and then dried at 70 °C under vacuum for 12 h.

[a]*College of Environmental Engineering, Xuzhou University of Technology, Xuzhou, 221018, China*

[b]*Li-ion Batteries Lab, School of Materials Science and Engineering, China University of Mining and Technology, Xuzhou 221116, China*

† Electronic supplementary information (ESI) available. See DOI: 10.1039/d1ra04869d

Physical characterization

The structure characterization of synthesized $KMnF_3$ prepared by co-precipitation method was analyzed by X-ray diffraction (XRD, D8 Discover, Bruker). The morphology and structure of cycled electrode samples were observed by transmission electron microscope (TEM, JEOL JSM-6700F, operated at 200 kV) and scanning electron microscopy (SEM, Magellan 400L, FEI). The element content is determined by inductively coupled plasma atomic emission spectrometer (ICP-OES).

Electrochemical performance characterization

Constant current charge and discharge tests were performed by using CR2025 coin cells. The electrochemical impedance spectroscopy test was tested with a three-electrode system. Pure potassium metal foil was used as the counter electrode and reference electrode and counter electrode. The frequency range of the EIS test is 10^5 to 10^{-2} Hz.

Results and discussion

First-principles calculation of $KMnF_3$

In this work, first-principles calculations are performed based on density functional theory (DFT) and the possibility of cubic $KMnF_3$ as a cathode for KIBs is predicted.

After complete geometric optimization, the lattice of cubic $KMnF_3$ is 4.15 Å, and that of cubic MnF_3 is 3.89 Å, as shown in Fig. S1.† It shows that the volume of the electrode material has a certain change during the charging and discharging process. The electric potential can be calculated using the following formula.

$$V = -\frac{E(KMnF_3) - E(MnF_3) - nE(K)}{nF}$$

In the formula, $E(KMnF_3)$ is the total energy of $KMnF_3$; $E(MnF_3)$ is the energy of MnF_3; $E(K)$ is the energy of K crystal; F is the Faraday constant; n is the number of K atoms in the redox reaction, where $n = 1$. The calculated potential value is 4.22 V. It can be seen that like most fluorides have a higher theoretical potential, the theoretical potential of cubic $KMnF_3$ converted to cubic MnF_3 is also higher than 4 V, which has inherent advantages as a cathode material.

Optimization of synthesis conditions

The addition of different solvents plays different roles in the synthesis process of the material, thereby changing the morphology and structure of the product. The solvent plays the role of changing the activation energy of the reaction during the reaction process, thereby promoting or inhibiting the formation of the product. Taking the common ethanol/water system as an example, the adjustment of the solvent ratio plays a crucial role in controlling the morphology of the product.[22,23]

In the co-precipitation system, from the perspective of the solubility of the reactants and products and the economics, distilled water is selected as the base solvent. The surface tension of ethanol and water are quite different, and the coefficient of surface tension of ethanol is about 1/3 of that of water, so the addition of ethanol will significantly reduce the critical size of nucleation. In order to observe the influence of different solvents more intuitively, a comparative study was carried out on pure distilled water and pure ethanol systems.

The TEM image and XRD image of the prepared $KMnF_3$ are shown in Fig. 1. In the distilled water system, the particle size formed is larger than 500 nm. It is mainly due to the large surface tension of water, which has a large critical nucleation size. In the ethanol system, the particle size of the formed particles is significantly reduced, but the particle size is

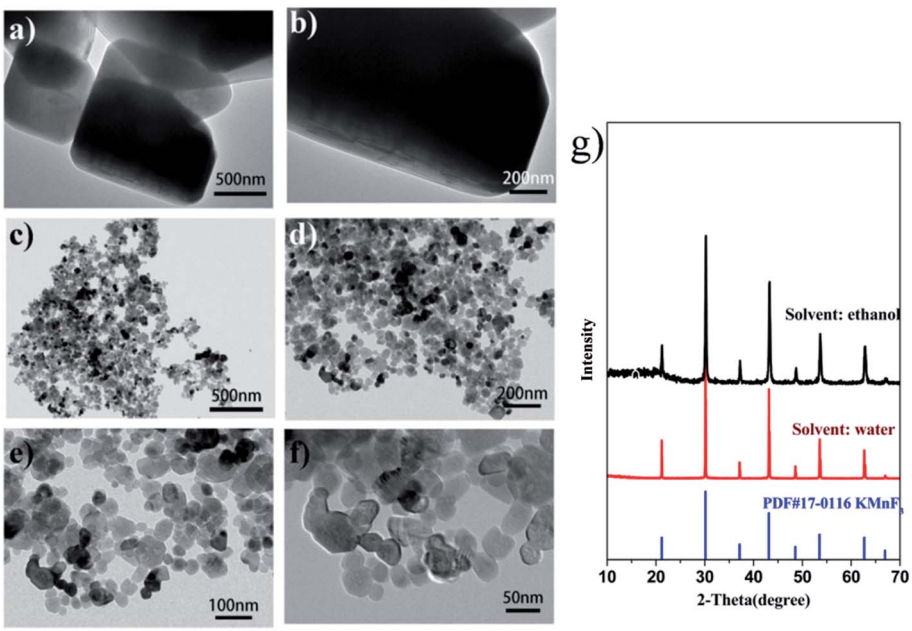

Fig. 1 TEM image of $KMnF_3$ prepared by distilled water solvent and ethanol solvent systems ((a and b) distilled water solvent; (c–f) ethanol solvent) and XRD image (g).

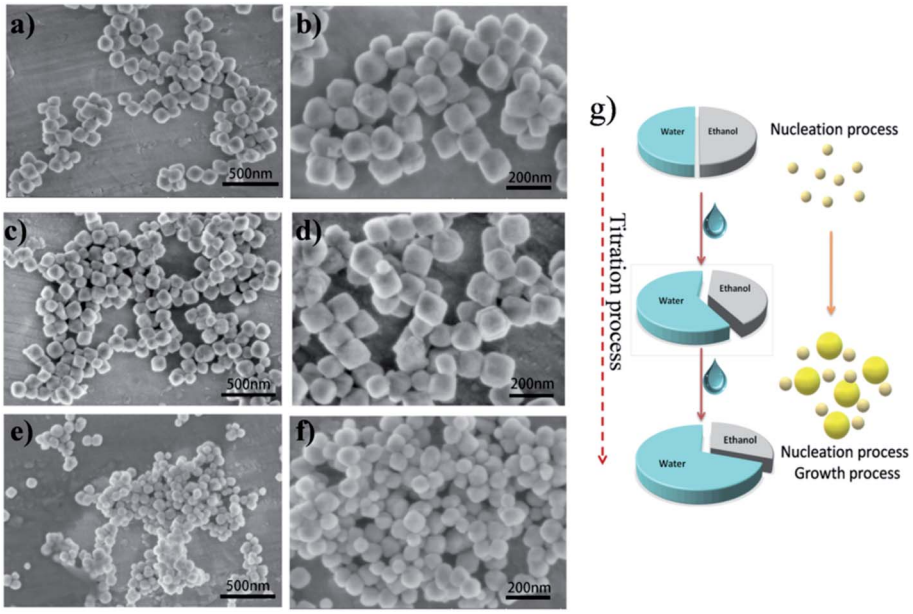

Fig. 2 SEM images of $KMnF_3$ prepared in mixed solvents with different proportions in potassium fluoride titration solution ((a and b) 1 : 1, (c and d) water, (e and f) ethanol) and schematic diagram of the process when the titration solution with water as solvent (g) Schematic diagram of the process when the solvent of KF titration is distilled water.

obviously uneven. Some particles have secondary agglomeration, indicating that the particle nucleation and growth process failed to achieve effective particle separation in this process. The lower surface tension of ethanol is conducive to the formation of smaller crystal nucleus, but it also increases the nucleation rate. A large number of crystal nuclei formed in an instant is difficult to achieve good dispersion. It can be seen that a single solvent fails to obtain a product with good morphological characteristics, and it is necessary to adjust the ratio of water and ethanol to form a mixed solvent.

Fig. S2† is an SEM image of $KMnF_3$ prepared in a mixed solvent (water and ethanol) system with different proportions. The addition of mixed solvents has a certain regulatory effect on the morphology of the synthesis process. The surface tension of the mixed solvent is moderate, and the size of the crystal nucleus can be well controlled to avoid instantaneous generation of a large number of crystal nuclei, which is conducive to the formation and dispersion of particles. When the ratio of water to ethanol is 2 : 1 and 1 : 2, there is still a certain amount of agglomeration, and good dispersion cannot be achieved. When the volume ratio of water to ethanol is 1 : 1, the obtained nanoparticles have a more uniform particle size and show better dispersibility. Therefore, the ratio of water to solvent in the mixed solvent is chosen to be 1 : 1.

In order to further optimize the reaction conditions of the co-precipitation process, the solvent ratio of the KF additive was also studied. The SEM images of $KMnF_3$ nanoparticles prepared with different solvent ratios of the additive solution are shown in Fig. 2a–f. When the solvent of the additive solution is ethanol, the lower surface tension of ethanol can reduce the critical size of nucleation and increase the nucleation rate sharply, triggering particle agglomeration. When the solvent of the additive liquid is distilled water, the schematic diagram of the process is shown in Fig. 2g. In the early stage of the titration process, when the additive liquid is in contact with the manganese acetate solution, the ethanol in the manganese acetate solution can be diluted to help provide an appropriate nucleation rate, and a controllable nucleation process will occur. As the titration process progresses, part of the nucleation process has been completed and then the growth process begins. At this time, the nucleation and growth processes coexist, and the process is complicated. With the continuous dripping of the additive liquid, it will have a continuous and slow inhibitory effect on the nucleation rate, which is extremely beneficial to the production of uniformly dispersed particles.

In order to understand the effect of the addition speed of the KF solution on the morphology of the prepared $KMnF_3$, the above-mentioned method of dropwise addition (1 drop per s) was changed to rapid addition (5 drops per s). The XRD and SEM analysis results of the sample synthesized by the rapid dropping method are shown in Fig. S3.† The XRD image shows that the product of the rapid dropping method is also $KMnF_3$ with a perovskite structure, and there is no impurity peak. The TEM image manifest that the morphology of the product is characterized by the interconnection and agglomeration of small particles to form several large particles. This result shows that the occurrence of the co-precipitation process is rapid, and the rapid stirring and slow dripping process are necessary to control the nucleation and growth process of particles.

In addition to the conditions that affect the co-precipitation process mentioned above, temperature is also one of the extremely important factors. In this experiment, three temperatures of 30 °C, 40 °C and 50 °C were selected for the conditional experiment, and the TEM image obtained is shown in Fig. 3.

The particle size of the particles obtained at 30 °C is about 100–120 nm, and a small amount of particles exhibit irregular morphology. It is presumed that the low temperature during the synthesis process and the slower ion diffusion rate make it impossible to complete the dispersion of all particles in a short time. When the temperature rises to 40 °C, the ion diffusion speed increases so that the dispersibility of the particles is improved to a certain extent, and the particle size distribution is uniform (about 100 nm). When the temperature rises to 50 °C, due to the further increase of ion diffusion rate, the further reduction of particle size leads to the exposure of highly active sites on the surface and the increase of collision probability between particles. These reasons all tend to cause partial agglomeration of particles. In summary, the nanoparticles prepared at 40 degrees have uniform particle size and good dispersibility, and the mapping results show that the F, K and Mn elements are uniformly distributed (Fig. 3j). The HRTEM image of $KMnF_3$ synthesized at 40 °C is shown in Fig. S4.† The interplanar spacing corresponds to the (100) crystal plane of $KMnF_3$.

Based on the comparison of the synthesis conditions of $KMnF_3$, it can be concluded that the synthesis conditions favorable to electrochemical performance are as follows. The volume ratio of water to ethanol in the solvent of manganese acetate solution is 1 : 1, the solvent of the potassium fluoride additive is distilled water, the titration rate is 1 drop per s, and the reaction temperature is 40°. The purity of the material was 98.5–99.2% after parallel sample test and calculation (due to the low solubility of $KMnF_3$ in water, it is necessary to dissolve it in a large amount of distilled water, and then use the ICP-OES method to determine the manganese ion content).

Electrochemical and interface performance test

Fig. S5† shows the charge and discharge curve of $KMnF_3$ cathode when the current density is 40 mA g^{-1} and the voltage range is 4.2–1.2 V *vs.* K^+/K. It can be seen from the curve that the initial charge and discharge capacity of $KMnF_3$ is relatively low, 70.5 and 47.6 mA h g^{-1}, respectively. The Coulomb efficiency in the first cycle is relatively low, and the capacity retention rate of the first few cycles is also relatively low. In order to explain the rapid decline of charge and discharge capacity, the Mn content in the electrolyte of the three-electrode glass electrolytic cell system was tested by ICP-OES under different cycles. The test results are shown in Fig. 4a. The change process of the SEI film after charging and discharging is illustrated in conjunction with Fig. 4b. After the first cycle of charge and discharge, the electrode material $KMnF_3$ has a certain amount of Mn dissolved in the electrolyte, but the dissolved amount is not high. The reason may be that a relatively complete SEI film was formed during

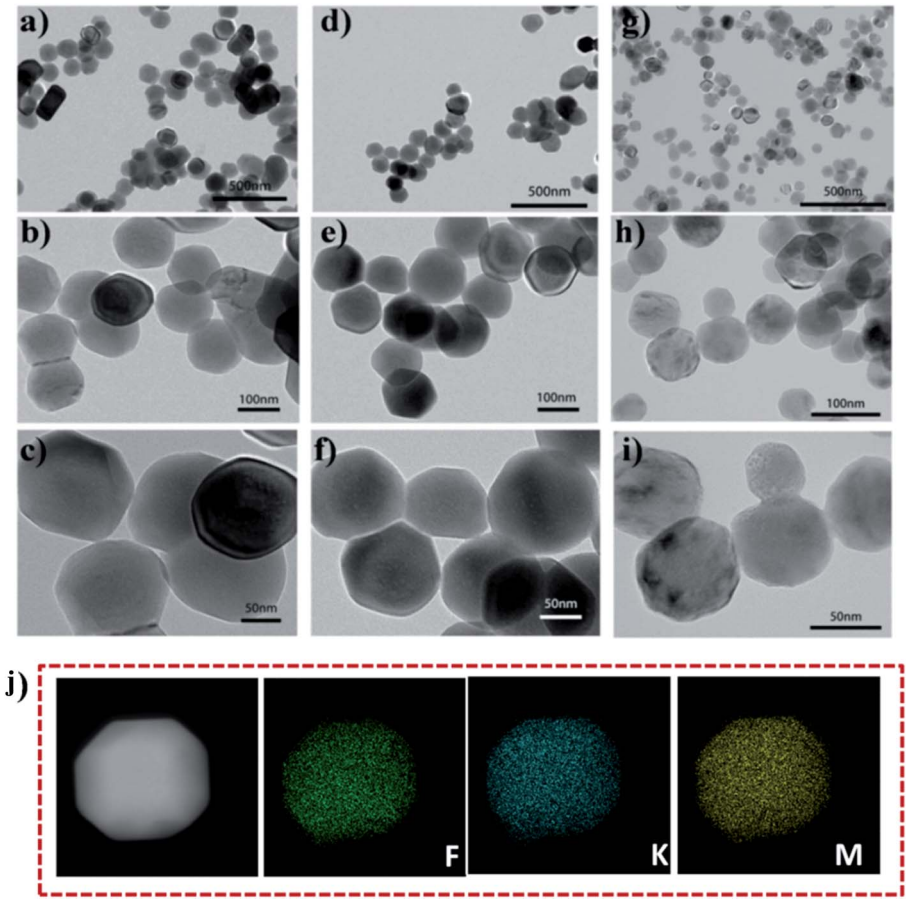

Fig. 3 a–i) TEM of $KMnF_3$ prepared at different temperatures ((a–c) 30 °C, (d–f) 40 °C, (g–i) 50 °C); (j) mapping of $KMnF_3$ prepared at 40 °C.

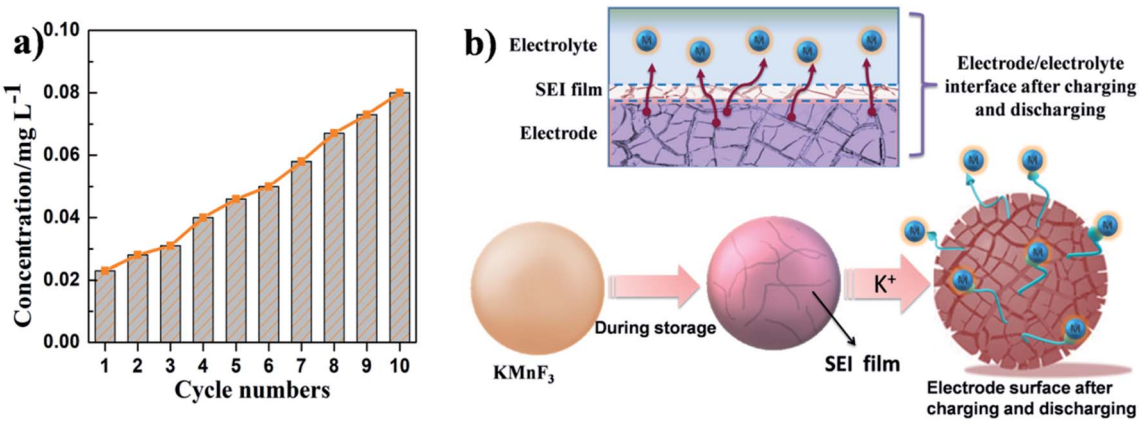

Fig. 4 (a) ICP-OES test results of manganese content of $KMnF_3$ electrode under different cycles. (b) Schematic illustration of the volume change of $KMnF_3$ cathode during the charge/discharge process: the volume change of the electrode material after repeated charging and discharging process causes the rupture of the interface SEI film, exposing part of the Mn ions to the electrolyte.

the standing process and the first cycle of charging and discharging, which inhibited the dissolution of Mn to a certain extent. As the charging and discharging continue, the volume change of the K^+ extraction and embedding process causes the SEI film to partially rupture. The Mn ions in the cracks not covered by the SEI film on the particle surface are exposed to the electrolyte, so that the dissolution of Mn in the electrolyte is significantly increased. This may be the reason for the degradation of the charge and discharge capacity. Although a higher charge and discharge capacity has not been obtained, it shows that the material can be charged and discharged at a higher voltage. The voltage comparison with other manganese-based electrode materials in the KIBs is shown in Table S1.†

Fig. S6a† shows the XRD pattern of the $KMnF_3$ cathode charged to different voltages for the first time. The different charging voltages all show XRD patterns similar to the original samples. The diffraction peak corresponding to $KMnF_3$ has no obvious diffraction peak position shift and intensity change. The XRD pattern after charging (Fig. S6b†) shows the change in the valence state of manganese. The above all indicate that the intercalation reaction of potassium occurs during the charging process.

It shows that the intercalation reaction of K occurs during the charging process. The following will study the interface characteristics through the EIS to reflect the key factors affecting the electrochemical performance of perovskite

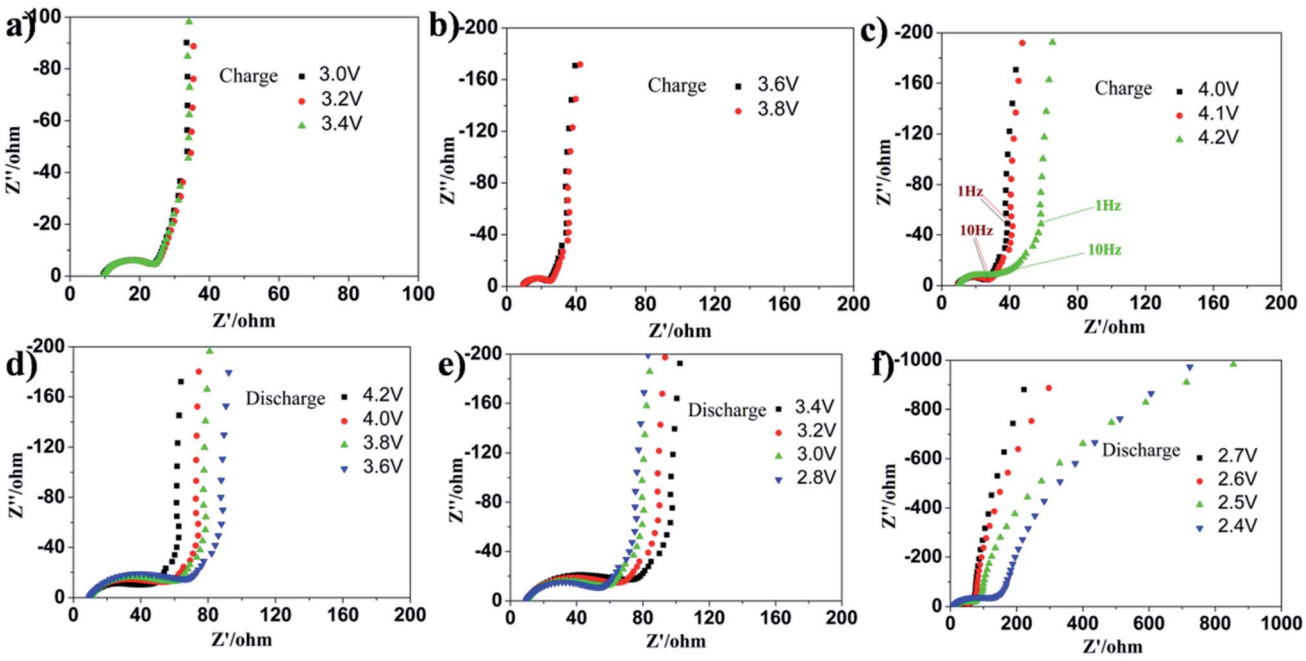

Fig. 5 Nyquist plots of $KMnF_3$ electrode at various potentials during the initial charge and discharge process ((a–c) the initial charge process, (d–f) the initial discharge process. The additional mark in (c) is the frequency value of the test point).

fluoride, and provide a theoretical basis for the subsequent improvement of electrochemical performance.

In order to study the electrode/electrolyte interface reaction process and explain the phenomenon of charging and discharging processes, the EIS of the $KMnF_3$ electrode was tested and shown in Fig. S7† and 5. In the entire voltage range, the Nyquist diagram consists of two parts, a semicircle in the high frequency area (HFS) and a slope or arc in the low frequency area (LFL/S). HFS can be attributed to the migration of K^+ through the SEI film covered by the active material. From the electrochemical impedance spectroscopy study of different self-discharge times shown in Fig. S7,† it can be seen that the SEI film formation process occurs during the self-discharge process, and a relatively stable SEI film is formed after 12 hours of self-discharge.

In order to verify the formation process of the SEI film, XPS tests before and after etching were performed on the electrode pads. Fig. S8† shows the XPS test results before and after the electrode is etched after self-discharge (etching thickness is 5 nm). In the C 1s spectrum, the C–O and C=O bond peaks are significantly reduced after the self-discharged electrode is etched, indicating that the SEI film has been formed at this time, and the thickness of the SEI film is small, which is close to the etched thickness.

Fig. 5 shows the Nyquist diagram during the first charge and discharge in the voltage range of 4.2–1.2 V *vs.* K^+/K. It can be seen that HFS only slightly changes at the beginning of charging, but the trend of HFS increase in the later stage of the charging process begins to increase (Fig. 5c). During the discharging process, as the discharging process progresses, the change of HFS will be more obvious (Fig. 5d–f), it shows that the SEI membrane is ruptured and regenerated obviously.

Based on the above experimental results, the equivalent circuit diagram of the $KMnF_3$ electrode impedance shown in Fig. 6 is proposed, which is used to indicate the EIS of the electrode during the charging and discharging process. In the equivalent circuit, R_s represents ohmic resistance, R_{SEI} and R_{ct} are SEI film resistance and charge transfer resistance, respectively, and SEI film capacitance and electric double layer capacitance are represented by constant phase angle elements Q_{SEI} and Q_{dl}, respectively. Fig. 6b shows the comparison between the test data of the EIS when discharged to 2.4 V and the fitted data obtained through the Zview software. The test data and the fitted data have good coincidence. The relevant parameter values of the equivalent circuit obtained by the fitting are shown in Table 1. The relative standard deviations of the fitted parameter values are all less than 15%, indicating that the circuit model selected here is basically consistent with the actual situation, and the data obtained by the fitting is reliable.

Fig. 6c shows the R_{SEI} curve of the $KMnF_3$ electrode obtained by Zview software during the initial charging and discharging process. In the initial stage of charging, R_{SEI} remained basically stable. From the high-voltage stage of charging to the subsequent discharging period, R_{SEI} exhibits an obvious alternating

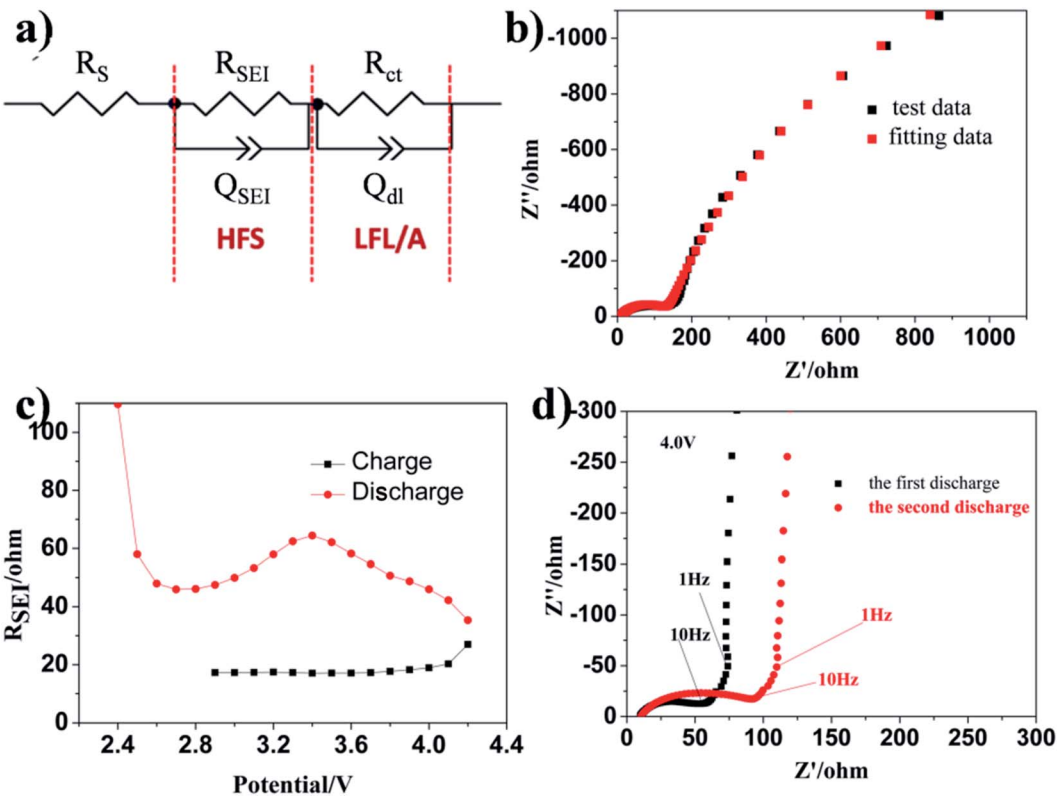

Fig. 6 (a) Equivalent circuit proposed for fitting EIS of $KMnF_3$ electrode, (b) comparison of test data and fitting data of EIS when discharged to 2.4 V, (c) variations of R_{SEI} with the electrode potential in the initial charge and discharge process, (d) comparison of EIS when discharged to 4.0 V in the first two cycles.

Table 1 Parameters of EIS fitting circuit when $KMnF_3$ electrode is discharged to 2.5 V

Parameters	Value	Error	Uncertainty%
R_s/Ω	9.227	0.09729	1.054
R_{SEI}/Ω	131.0	1.765	1.348
Q_{SEI}-n	1.541×10^{-4}	7.022×10^{-6}	4.556
Q_{SEI}-Y_0	0.6846	5.856×10^{-3}	0.8554
R_{ct}/Ω	3776	137.73	3.648
Q_{dl}-n	3.111×10^{-3}	3.207×10^{-5}	1.031
Q_{dl}-Y_0	0.8500	6.944×10^{-3}	0.8168

increasing and decreasing trend. The above phenomenon is usually attributed to the reversible formation and decomposition of the SEI film covering the cathode during charge and discharge.[24] Since the SEI film covers the surface of the particles, the continuous formation and decomposition of the SEI film may cause a large amount of Mn ions to directly contact the electrolyte, which is not conducive to obtaining good cycle performance. Fig. 6d shows the comparison of EIS when discharged to 4.0 V in the first two cycles. Compared with the first cycle, the HFS in the EIS of the second cycle increased significantly, which is one of the reasons for the capacity degradation during the cycle. In order to verify the influence of the different morphologies of $KMnF_3$ (optimal conditions and fast titration conditions) on the formation of SEI film and the dissolution of Mn in the electrolyte, electrochemical impedance spectroscopy was used to compare the SEI film, and ICP-OES was used to measure the electrode material in the electrolyte after the charge and discharge cycle (Fig. S9 and Table S2†). This shows that the electrode material synthesized under the optimized conditions has uniform particle size and good dispersibility, which is conducive to the formation of a uniform SEI film, and the uniform SEI film will not be repeatedly ruptured and regenerated during repeated charging and discharging, thereby preventing manganese ions.

LFL/S is related to the charge transfer process, and there is no obvious tendency to bend and form an arc during the entire charging process, which is mainly due to the high charge transfer resistance.[25–27] The charge transfer resistance is also an important parameter that affects the electrochemical performance of this fluoride material.

Conclusions

In this paper, the perovskite fluoride $KMnF_3$ is selected as the cathode for KIBs. First, the feasibility of $KMnF_3$ as a cathode for KIBs is calculated using first principles. The calculation results show that $KMnF_3$ has a theoretical potential higher than 4 V and has inherent advantages as a cathode. Cubic $KMnF_3$ nanomaterials with uniform particle size distribution and about 100 nm were synthesized by a co-precipitation method. The synthesis conditions were optimized and the formation mechanism of nanomaterials was speculated. The EIS test confirmed the formation process of the SEI film and study the main factors affecting the charge and discharge performance. On the one hand, the R_{SEI} exhibits an obvious alternating increase and decrease trend, indicating that the SEI film is continuously formed and decomposed during the charge and discharge process, which makes the irreversible capacity increase. On the other hand, the continuous formation and decomposition of the SEI film will also cause the Mn ions in the electrode material to directly contact the electrolyte, which is not conducive to obtaining good cycle performance. In addition, the charge transfer resistance may be an important parameter that affects the electrochemical performance of this fluoride material. Based on the above analysis, theoretical guidance is provided for the improvement of the electrochemical performance of such materials.

Conflicts of interest

There are no conflicts to declare.

Acknowledgements

This work was supported by the National Natural Science Foundation of China (No. 22006125).

References

1 X. Hua, A. Eggeman, E. Castillo-Martinez, R. Robert, H. Geddes, Z. Lu, C. Pickard, W. Meng, K. Wiaderek, N. Pereira, G. Amatucci, P. Midgley, K. Chapman, U. Steiner, A. Goodwin and C. Grey, *Nat. Mater.*, 2021, **20**, 841–850.
2 K. Shimoda, M. Shikano, M. Murakami and H. Sakaebe, *J. Power Sources*, 2020, **477**, 228772.
3 D. Cao, C. Yin, D. Shi, Z. Fu, J. Zhang and C. Li, *Adv. Funct. Mater.*, 2017, **27**, 1701130.
4 A. Kitajou, H. Komatsu, K. Chihara, I. D. Gocheva, S. Okada and J.-i. Yamaki, *J. Power Sources*, 2012, **198**, 389–392.
5 A. Kitajou, Y. Ishado, T. Yamashita, H. Momida, T. Oguchi and S. Okada, *Electrochim. Acta*, 2017, **245**, 424–429.
6 I. D. Gocheva, M. Nishijima, T. Doi, S. Okada, J. I. Yamaki and T. Nishida, *J. Power Sources*, 2009, **187**, 247–252.
7 M. Kong, K. Liu, J. Ning, J. Zhou and H.-H. Song, *J. Mater. Chem. A*, 2017, **5**, 19280–19288.
8 D. Cao, C. Yin, D. Shi, Z. Fu, J. Zhang and C. Li, *Sci. Found. China*, 2017, **27**, 1701130.
9 K. S. Aleksandrov and V. V. Beznosikov, *Phys. Solid State*, 1997, **39**, 695–715.
10 L. Zhang, W. A. Wang, X. Ma, S. Lu and Y. Xiang, *Nano Today*, 2021, **37**, 101074.
11 Y. Wang, P. Niu, J. Li, S. Wang and L. Li, *Energy Storage Mater.*, 2021, **34**, 436–460.
12 Y. Zhang, X. Niu, L. Tan, L. Deng, S. Jin, L. Zeng, H. Xu and Y. Zhu, *ACS Appl. Mater. Interfaces*, 2020, **12**, 9332–9340.
13 D.-H. Liu, W.-H. Li, Y.-P. Zheng, Z. Cui, X. Yan, D.-S. Liu, J. Wang, Y. Zhang, H.-Y. Lü, F.-Y. Bai, J.-Z. Guo and X.-L. Wu, *Adv. Mater.*, 2018, **30**, 1706317.

14 D. S. Liu, D. H. Liu, B. H. Hou, Y. Y. Wang, J. Z. Guo, Q. L. Ning and X. L. Wu, *Electrochim. Acta*, 2018, **264**, 292–300.
15 Y. Qiong, W. Peng-Fei, G. Jin-Zhi, C. Zi-Ming, P. Wei-Lin, H. Ke-Cheng, G. Yu-Guo, W. Xing-Long and Z. Jingping, *ACS Appl. Mater. Interfaces*, 2018, **10**, 34272–34282.
16 Q. Ma, Q. Deng, H. Sheng, W. Ling, H. R. Wang, H. W. Jiao, X. W. Wu, W. X. Zhou, X. X. Zeng, Y. X. Yin and Y. G. Guo, *Sci. China: Chem.*, 2018, **61**, 732–738.
17 C. Vaalma, G. A. Giffin, D. Buchholz and S. Passerini, *J. Electrochem. Soc.*, 2016, **163**, A1295–A1299.
18 H. Kim, D.-H. Seo, J. C. Kim, S.-H. Bo, L. Liu, T. Shi and G. Ceder, *Adv. Mater.*, 2017, **29**, 1702480.
19 Q. Zhang, Z. Wang, S. Zhang, T. Zhou, J. Mao and Z. Guo, *Electrochem. Energy Rev.*, 2018, **1**, 625–658.
20 S. Rüdiger, G. Eltanany, U. Groß and E. Kemnitz, *J. Sol-Gel Sci. Technol.*, 2007, **41**, 299–311.
21 Y. Shi, S. Sun, J. Liu, Y. L. Cui, Q. C. Zhuang and X. Chen, *RSC Adv.*, 2016, **6**, 61–66.
22 X. W. Lou, Y. Wang, C. Yuan, J. Y. Lee and L. A. Archer, *Adv. Mater.*, 2006, **18**, 2325–2329.
23 I. S. Khattab, F. Bandarkar, M. A. A. Fakhree and A. Jouyban, *Korean J. Chem. Eng.*, 2012, **29**, 812–817.
24 A. J. Gmitter, F. Badway, S. Rangan, R. A. Bartynski, A. Halajko, N. Pereira and G. G. Amatucci, *J. Mater. Chem.*, 2010, **20**, 4149–4161.
25 H. Nara, K. Morita, D. Mukoyama, T. Yokoshima, T. Momma and T. Osaka, *Electrochim. Acta*, 2017, **241**, 323–330.
26 H. Nara, D. Mukoyama, T. Yokoshima, T. Momma and T. Osaka, *J. Electrochem. Soc.*, 2016, **163**, A434–A441.
27 M. Holzapfel, A. Martinent, F. Alloin, B. L. Gorrec, R. Yazami and C. Montella, *J. Electroanal. Chem.*, 2003, **546**, 41–50.